Supporting Information

Ultra-durable Ni-Ir/$MgAl_2O_4$ catalysts for dry reforming of methane enabled by dynamic balance between carbon deposition and elimination

Table of Contents

Catalyst preparation

The $MgAl_2O_4$ support was synthesized by the hydrothermal method [1]. The specific steps are as follows: 18.0 mmol aluminum isopropoxide and 9.0 mmol $Mg(NO_3)_2 \cdot 6H_2O$ were added to 55 mL of absolute ethanol. After stirring for 30 min, the mixture was transferred into a 200 mL polytetrafluoroethylene-lined stainless steel tubular reactor. After reacting at 150 ºC for 12 hours, the liquid was removed by rotary evaporation, and the powder obtained dried in a vacuum drying oven at 60 ºC overnight. The powder calcinated in a muffle furnace at 800 ºC for 12 hours at a heating rate of 2 $^oC \cdot min^{-1}$. The white powdery solid was the $MgAl_2O_4$ spinel.

The Ni-Ir/$MgAl_2O_4$ catalyst was prepared by the impregnation method. The $Ni_3Ir_x/MgAl_2O_4$ catalysts with a Ni loading of 3 wt% (x/3 represents the molar ratio relative to Ir/Ni) were prepared by the co-impregnation method. $Ni(NO_3)_2 \cdot 6H_2O$ and $IrCl_3 \cdot xH_2O$ were dissolved in deionized water. The $MgAl_2O_4$ spinel was added into the mixed solution of precursors under stirring for 12 hours at room temperature, and then rotate to remove the water. The powder obtained dried in a vacuum drying oven at 60 ºC overnight, and then calcinated in a muffle furnace at 550 ºC for 4 hours at a heating rate of 2 $^oC \cdot min^{-1}$. The content of Ir in $Ir/MgAl_2O_4$ was 3wt%.

Catalytic evaluation

The performance evaluation for methane dry reforming was performed in a four-channel fixed-bed flow reactor, which used four identical quartz reaction tubes. The catalyst powder was pressed into tablets, and particles of 40-60 mesh were screened out by crushing. 60 mg of catalyst particles were weighed, mixed with 300 mg of 40-60 mesh quartz sand, and then put into a quartz reaction tube. The total flow of H_2, N_2, CH_4, and CO_2 was controlled by the corresponding mass flow meter (MFC). The flow distribution system was used to divide the gas flow into four evenly, which were introduced into the four reaction tubes. A two-stage electric heating furnace was used

to heat the reaction tube. The catalyst was located in the constant temperature zone of the heating furnace. The exhaust gas passed through a cold trap to condense the water vapor. The selected exhaust gas flowed through the quantitative ring of the electric six-way valve, and then was discharged to the outdoor high altitude. The composition and content of the exhaust gas were analyzed by a Shimadzu GC-2014 chromatographic automatic sample injection analysis. A 60 cm long TDX-01 packed column with an inner diameter of 2 mm was used to separate the components, and the TCD was used as a detector. The detection time was 10 minutes, and the four-way exhaust gas was analyzed in turn.

Before the reaction, the catalyst was reduced with 30 $mL \cdot min^{-1}$ high-purity hydrogen at 650 ºC for 2 hours, and the heating rate was 10 $ºC \cdot min^{-1}$. After the reduction was complete, purge with nitrogen for 10 minutes to desorb the hydrogen adsorbed on the catalyst surface. Then turn off N_2, and pass in CH_4 and CO_2. The flow rate of methane was $F_{CH_4} = 33.3$ $mL \cdot min^{-1}$, and the flow rate of carbon dioxide was $F_{CO_2} = 33.3$ $mL \cdot min^{-1}$. After the reactor was cooled to room temperature, the catalyst was taken out and separated from quartz sand for subsequent analysis and characterization.

The conversion of CH_4, CO_2, and H_2/CO were calculated by the following formula:

The conversion of CH_4: $C_{CH_4} = \frac{F_{CH_{4,in}} - F_{CH_{4,out}}}{F_{CH_{4,in}}} \times 100\%$ (1)

The conversion of CO_2: $C_{CO_2} = \frac{F_{CO_{2,in}} - F_{CO_{2,out}}}{F_{CO_{2,in}}} \times 100\%$ (2)

The H_2/CO: $\frac{n_{H_2}}{n_{CO}} = \frac{F_{H_{2,out}}}{F_{CO_{out}}}$ (3)

F: Gas flow ($mL \cdot min^{-1}$),

In: Reactor inlet,

Out: Reactor outlet.

Structural characterization

Nitrogen adsorption-desorption. Quantachrome Autosorb-3B adsorption instrument was used for nitrogen adsorption-desorption test. The test and analysis methods were as follows: the sample was vacuum-activated at 300 ºC for 3 hours, and then nitrogen

was adsorbed and desorbed in a liquid nitrogen bath (77 K) to obtain an isotherm. The Brunauer-Emmet-Teller (BET) method was used to calculate the specific surface area:

$$\frac{P}{V(P_0-P)} = \frac{1}{V_m C} + \frac{(C-1)P}{W_m C P_0} \quad (4)$$

$$S_g = 4.353 V_m \ \text{m}^2/\text{g}$$

The Barrett-Jovner-Halenda (BJH) method was used to calculate the pore size distribution of the adsorption-desorption isotherm desorption branch.

X-ray diffraction. Japan Rigaku Ultima X-ray diffractometer was used for phase analysis of catalyst samples. The radiation source adopted Cu Kα line with wavelength λ = 0.15405 nm, and used Goebel mirror to converge the divergent X beam into parallel light. The tube voltage was 35 kV, the tube current was 25 mA, the scanning rate was 10 º/min, and the scanning step length was 0.02 º. According to the Bragg formula:

$$2d_{(hkl)} \sin\theta_{(hkl)} = \lambda \quad (5)$$

From the position $2\theta_{(hkl)}$ of the diffraction peak (hkl) on the XRD pattern, the corresponding interplanar distance $d_{(hkl)}$ could be calculated, and then the unit cell parameters of the sample could be obtained according to $d_{(hkl)}$.

The half-width of the XRD diffraction of the sample and the grain size of the sample accorded with the Scherrer formula:

$$D = K\lambda/\beta\cos\theta \quad (6)$$

Among them, D is the grain size, λ is the wavelength of incident X-ray, and λ = 0.15405 nm in this paper. K is the grain shape factor, taking K = 0.89. β is the half-width of the diffraction peak. In order to eliminate the influence of instrument factors on the width of the diffraction peak, the instrument is calibrated with quartz as the reference material:

$$\beta_t = \sqrt{\beta_o^2 - \beta_{Quartz}^2} \quad (7)$$

β_o: measured half-width,

β_{Quartz}: half-width of the quartz sand near the diffraction peak of the sample.

X-ray photoelectron spectroscopy. A Thermo Scientific K-Alpha X-ray photoelectron spectrometer was used to collect the X-ray photoelectron spectroscopy data of the catalyst. The binding energy of C1s (284.8 eV) was used for correction.

Transmission electron microscope. The US FEI-Tecnai G2F30 field emission electron microscope was used to observe the catalyst microstructure and sample image

collection. The Oxford X-Max T80 energy spectrometer configured on the electron microscope was used for surface scan and line scan data acquisition.

Scanning electron microscope. The Hitachi S-4800 scanning electron microscope was used to observe the morphology of the catalyst and to collect the image of the sample.

Raman spectroscopy. It was performed by DXR2 Raman Spectrometer with 532 nm laser. It was used to analyze the coking of samples.

Thermogravimetric Analysis. A METTLER TOLEDO thermogravimetric analyzer was used to characterize the carbon deposits of the spent catalyst. The test conditions: about 5 mg of the spent catalyst powder, at an air flow rate of 50 mL/min, rising from 25 ºC to 800 ºC at a heating rate of 10 ºC·min^{-1}.

Diffuse reflectance infrared fourier transform spectroscopy. Operando DRIFTS measurements were performed by BRUKER TENSOR 27 with a Harrick cell and an MCT detector. The resolution of infrared spectrum collection was 4 cm^{-1}, and the number of collections was 64 times. Before the experiment, the sample was pre-treated in the in-situ cell in an H_2 atmosphere at 650 °C for 1 hour, and then switched to an Ar atmosphere for 30 minutes to eliminate surface adsorbed substances. The background spectrum of the sample was collected under Ar atmosphere. In the first stage, pass CO_2 (50 mL·min^{-1}) into the in-situ cell to react for 15 minutes and collect the sample spectrum (30 s/spectrum), and then purge by Ar until there was no gaseous CO_2 in the collected sample spectrum. In the second stage, CH_4 (50 mL·min^{-1}) was passed into the in-situ cell for 15 minutes to react and the spectrum of the sample was collected (30s/spectrum), and then purge by Ar until there was no gaseous CO_2 in the collected sample spectrum. In the third stage, CO_2 (50 mL·min^{-1}) was introduced into the in-situ tank to react for 15 minutes and the sample spectrum was collected (30 s/spectrum).

Temperature programmed surface reaction-mass spectrum. It was carried out on the Tianjin Xianquan TP5080 multi-purpose adsorption apparatus with a thermal conductivity detector (TCD). The test procedure for CH_4 dissociation: 30 mg of a sample with a particle size of 20-40 mesh, pretreat it at 650 ºC for 1 hour under 30 mL·min^{-1} H_2 purge. Then cool down to room temperature (approximately 25 ºC), and switch the H_2 to 5 mL·min^{-1} CH_4 to record mass baseline. After the baseline is stable,

the temperature is increased to 650 ºC at a heating rate of 10 ºC·min^{-1} and then kept for 1 h, while the mass spectrum was recorded at the same time. Then switch CH_4 to 30 mL·min^{-1} N_2 and cool down to room temperature (about 25 ºC). Switch the N_2 to 5 mL·min^{-1} CO_2 and start to record the mass spectrum baseline. After the baseline is stable, the temperature is increased to 950 ºC at a heating rate of 10 ºC·min^{-1}, and the mass spectrum is recorded.

CO_2-temperature programmed desorption. It was carried out on the Tianjin Xianquan TP5080 multi-purpose adsorption apparatus with a thermal conductivity detector (TCD). The test procedure: 30 mg of a sample with a particle size of 20-40 mesh, pretreat it at 300 ºC for 1 hour under 30 mL·min^{-1} He purge. Then cool down to room temperature (approximately 25 ºC), and switch the He to 30 mL·min^{-1} CO_2 for 1h. After that, switch the CO_2 to 30 mL·min^{-1} He and start recording the baseline. After the baseline is stable, stop recording. Then increase the temperature to 900 ºC at a heating rate of 10 ºC·min^{-1}, and record the reduction curve at the same time.

Computational details.

Spin-polarized periodic density functional theory (DFT) calculations were implemented using the Vienna Ab Initio Simulation Package (VASP) software[2-5]. The generalized gradient approximation (GGA) of Perdew-Burke-Ernzerh (PBE) exchange-correlation functional[6], using projector-augmented wave (PAW) pseudopotentials [7], was employed here. Grimme's DFT-D3BJ approach[8] was also involved to describe van der Waals interactions between the molecules and the catalyst surfaces. The valence electrons were described by plane wave basis sets with a plane-wave cut-off energy of 400 eV, whereas the energy and residual forces during the optimization were converged to 10^{-5} eV and 0.05 eV/Å, respectively. The spinel $MgAl_2O_4$ unit cell was calculated through a 6×6×6 k-point grid, and a p(2×2) superstructure was employed for simulating the $MgAl_2O_4$ (100) surface with eight layers in which the bottom five layers of atoms were fully fixed and the other atoms were allowed to relax during the optimization. The vacuum region was set to 20 Å for the slab model. The Brillouin zone sampling was

conducted with the Gamma point. The climbing nudged elastic band (CINEB) method [9-10] and the dimer method [11] were applied for optimizing transition states (TS). Adsorption energies of CO_2, CO and O-atom were calculated by the following formula:

$$\Delta E_{ads,CO2} = E_{catalyst+CO2} - E_{catalyst} - E_{CO2} \quad (8)$$

$$\Delta E_{ads,CO} = E_{catalyst+CO2} - E_{catalyst} - E_{CO} \quad (9)$$

$$\Delta E_{ads,CO} = E_{O2} - E_{catalyst} - 0.5\, E_{O2} \quad (10)$$

where $E_{ads,CO2}$, $E_{ads,CO}$, $E_{ads,O}$ are the total energies for the adsorbed CO_2, CO and O-atom on the catalyst, respectively, $E_{catalyst}$ is the energy of the unabsorbed catalyst, and E_{CO2}, E_{CO} and E_{O2} are the energies of CO_2, CO and O_2, respectively.

Figures

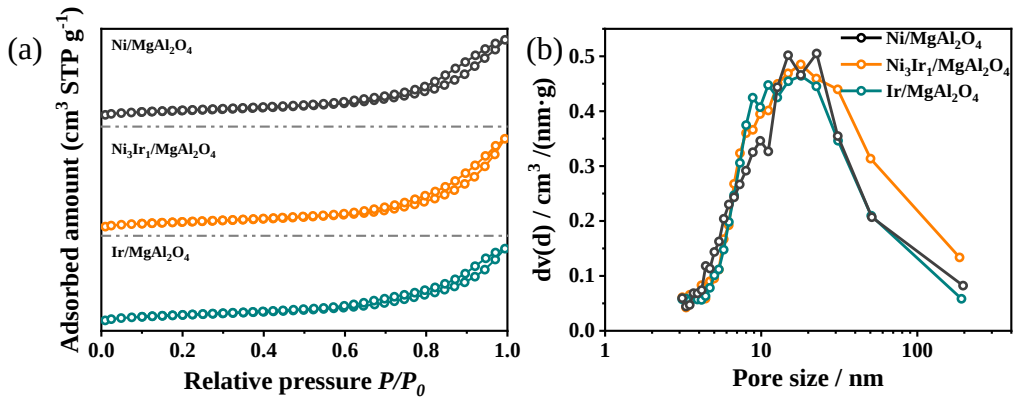

Fig. S1 (a) N_2 adsorption–desorption isotherms and (b) pore size distribution plots for $Ni/MgAl_2O_4$, $Ni_3Ir_1/MgAl_2O_4$, and $Ir/MgAl_2O_4$.

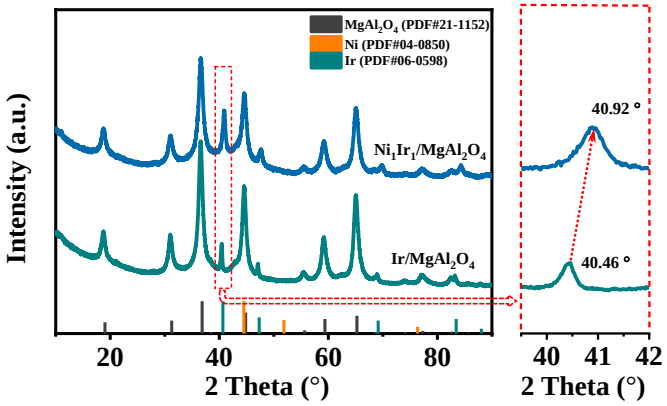

160

161 Fig. S2 XRD patterns of $Ni_1Ir_1/MgAl_2O_4$, and $Ir/MgAl_2O_4$.

162

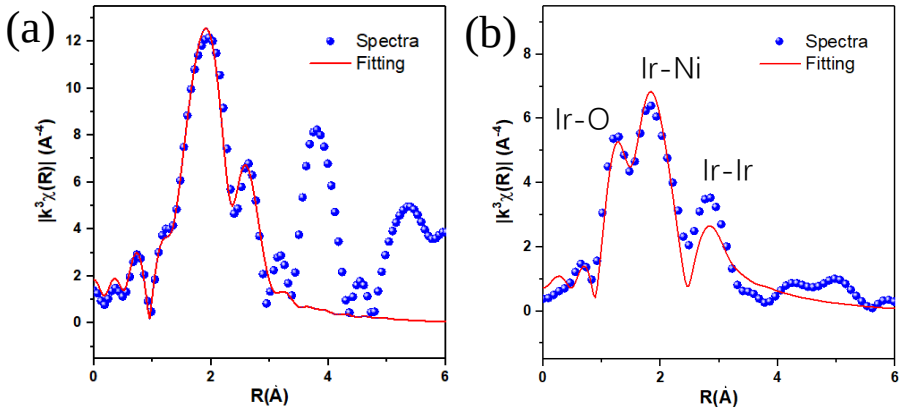

Fig. S3 (a) Ni and (b) Ir K edge X-ray adsorption fine structure (XAFS) spectroscopy analysis of the $Ni_3Ir_1/MgAl_2O_4$ catalyst.

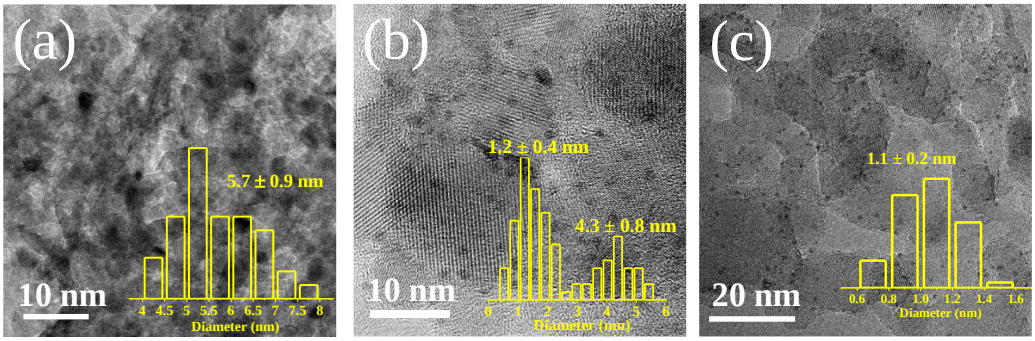

Fig. S4 HRTEM images for fresh catalysts of (a) $Ni/MgAl_2O_4$, (b) $Ni_3Ir_1/MgAl_2O_4$ and (c) $Ir/MgAl_2O_4$.

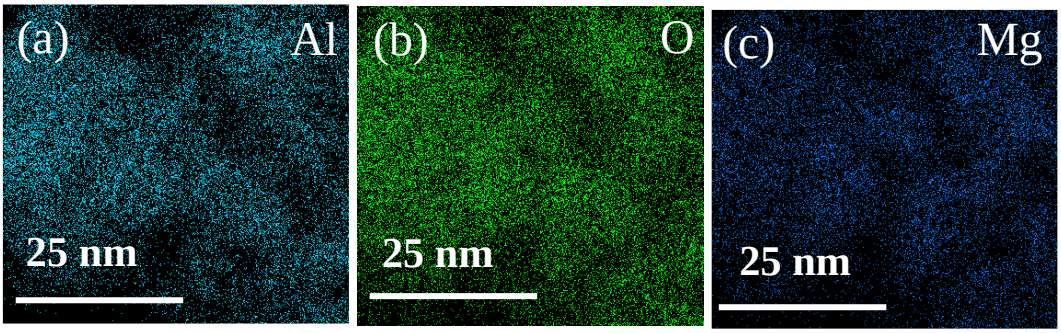

Fig. S5 TEM-mapping of the $Ni_3Ir_1/MgAl_2O_4$ catalyst; (a) Al, (b) O, and (c) Mg.

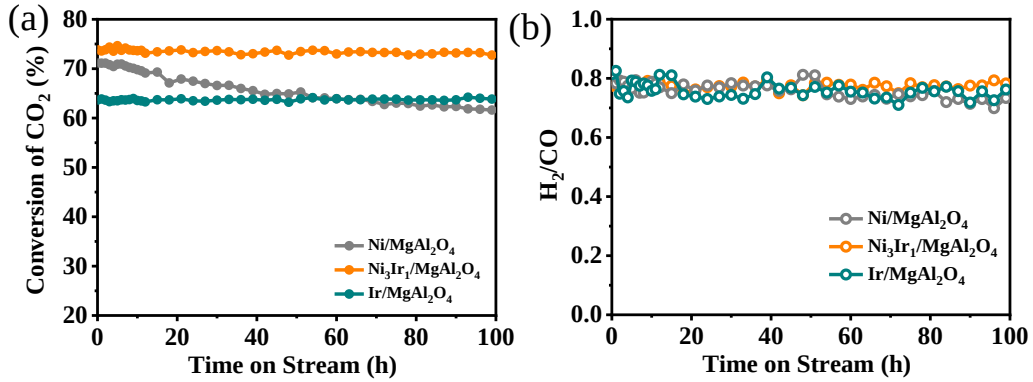

Fig. S6 (a) CO_2 conversion and (b) H_2/CO ratio for $Ni/MgAl_2O_4$, $Ni_3Ir_1/MgAl_2O_4$, and $Ir/MgAl_2O_4$. Reaction conditions: 650 °C, CH_4/CO_2 = 1/1, GHSV = 40,000 $mL \cdot g^{-1} \cdot h^{-1}$, and 1 atm.

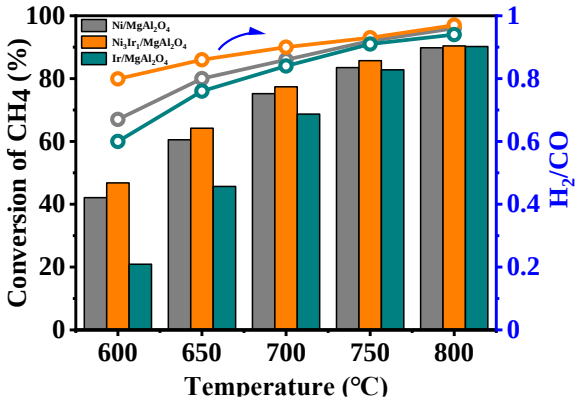

Fig. S7 CH_4 conversion and H_2/CO ratio for $Ni/MgAl_2O_4$, $Ni_3Ir_1/MgAl_2O_4$, and $Ir/MgAl_2O_4$ from 600 to 800 °C.

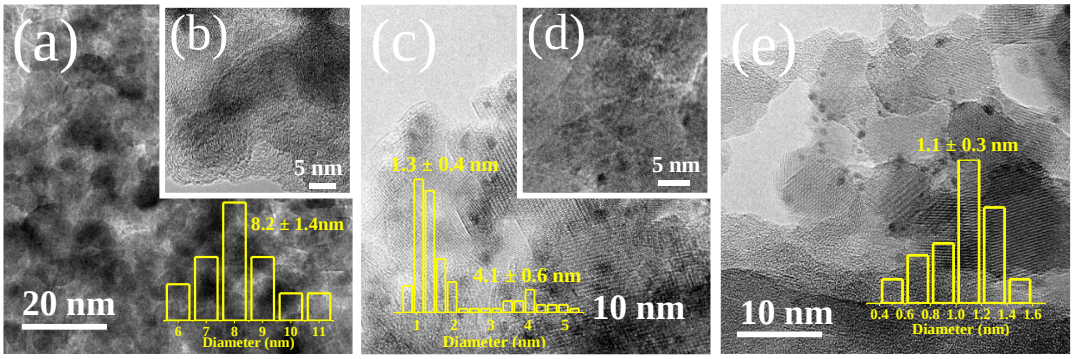

Fig. S8 HRTEM images for spent catalysts of (a-b) $Ni/MgAl_2O_4$, (c-d) $Ni_3Ir_1/MgAl_2O_4$ and (e) $Ir/MgAl_2O_4$.

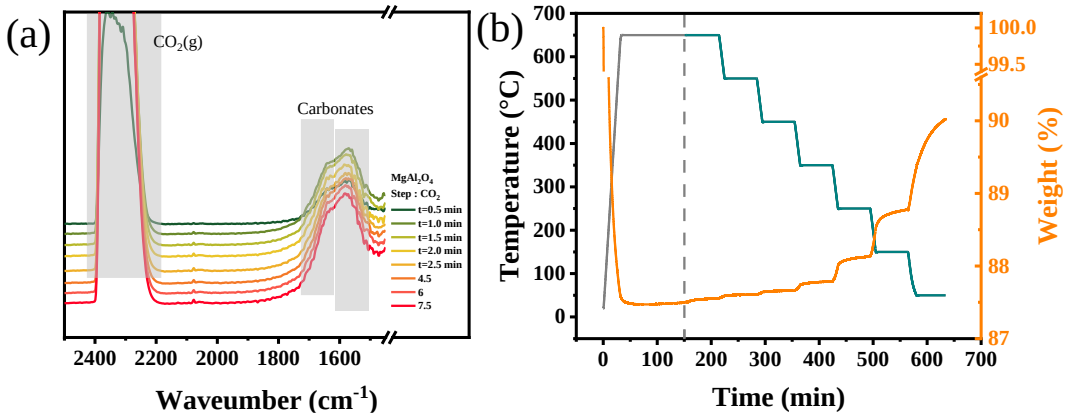

Fig. S9 (a) The in-situ DRIFTS spectra of $MgAl_2O_4$ after the introduction of CO_2, (b) adsorption capacity of CO_2 on $MgAl_2O_4$ from 650 to 50 °C.

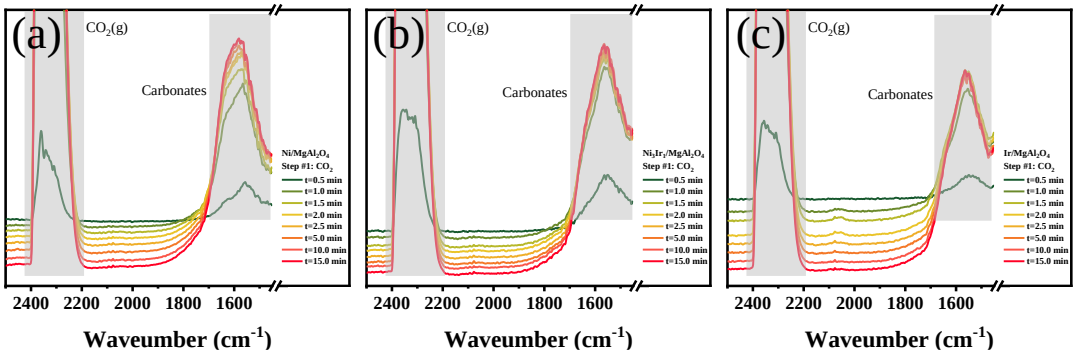

Fig. S10 In-situ DRIFTS spectra after introduction of CO_2 for (a) $Ni/MgAl_2O_4$, (b) $Ni_3Ir_1/MgAl_2O_4$, and (c) $Ir/MgAl_2O_4$.

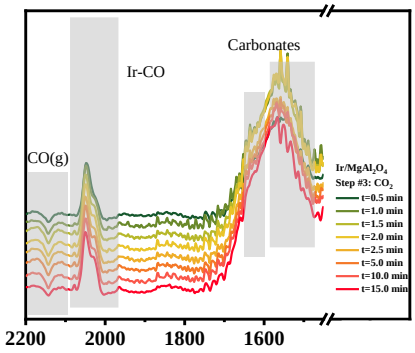

Fig. S11 In-situ DRIFTS spectra after the reintroduction of CO_2 in the third stage of testing for $Ir/MgAl_2O_4$ with prolonged CH_4 exposure.

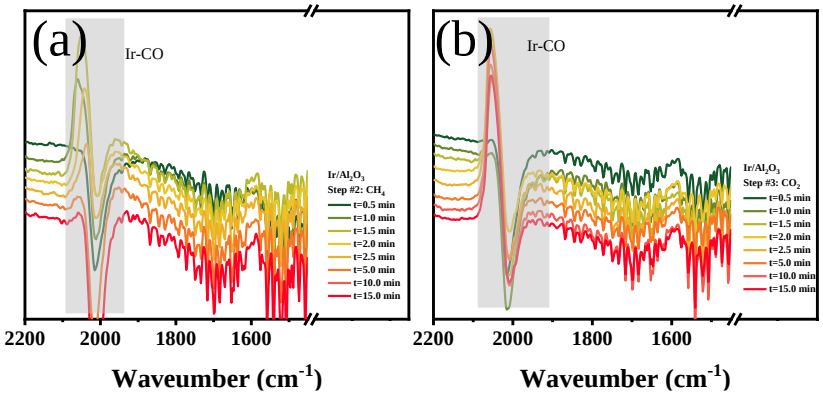

Fig. S12 In-situ DRIFTS spectra after (a) introduction of CH_4 in the second stage, and (b) introduction of CO_2 in third stage for Ir/Al_2O_3.

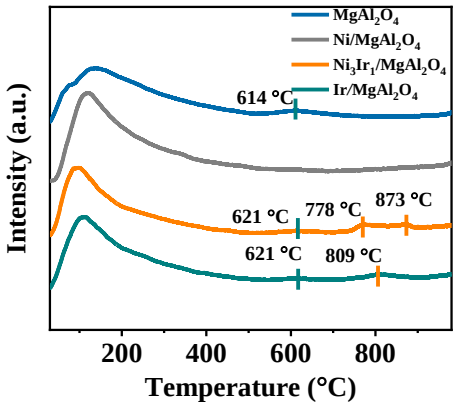

Fig. S13 Temperature programmed desorption of CO_2 (CO_2-TPD) for $Ni/MgAl_2O_4$, $Ni_3Ir_1/MgAl_2O_4$, $Ir/MgAl_2O_4$, and $MgAl_2O_4$.

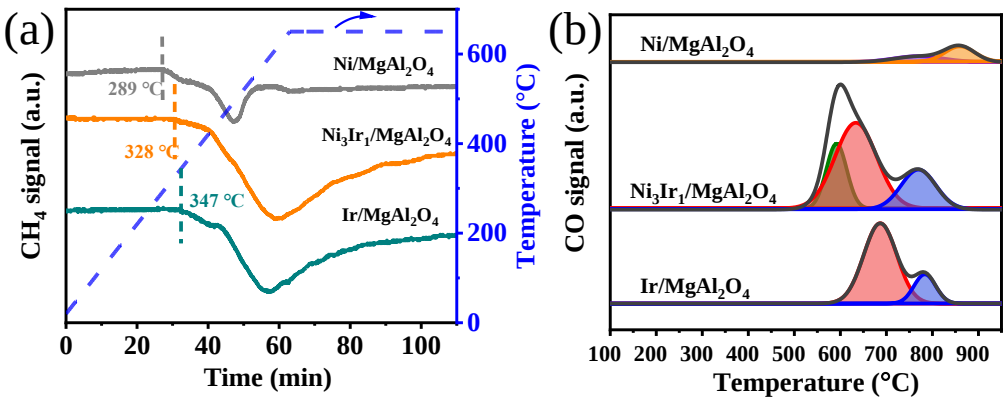

Fig. S14 The mass spectra of TPSR for $Ni/MgAl_2O_4$, $Ni_3Ir_1/MgAl_2O_4$, and $Ir/MgAl_2O_4$ (a) introduction of CH_4, (b) introduction of CO_2 after CH_4.

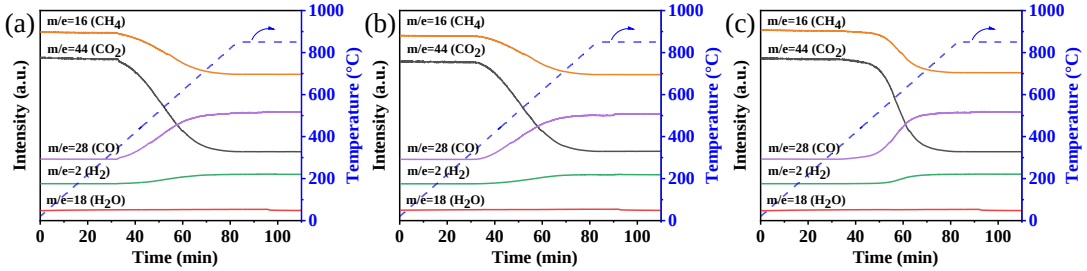

Fig. S15 The mass spectra for CH_4, CO_2, CO, H_2, and H_2O during TPSR with CH_4 for (a) $Ni/MgAl_2O_4$, (b) $Ni_3Ir_1/MgAl_2O_4$, and (c) $Ir/MgAl_2O_4$.

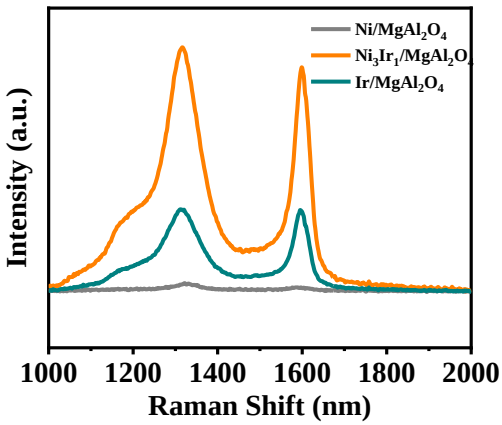

Fig. S16 The Raman spectra of $Ni/MgAl_2O_4$, $Ni_3Ir_1/MgAl_2O_4$, and $Ir/MgAl_2O_4$ after TPSR with CH_4.

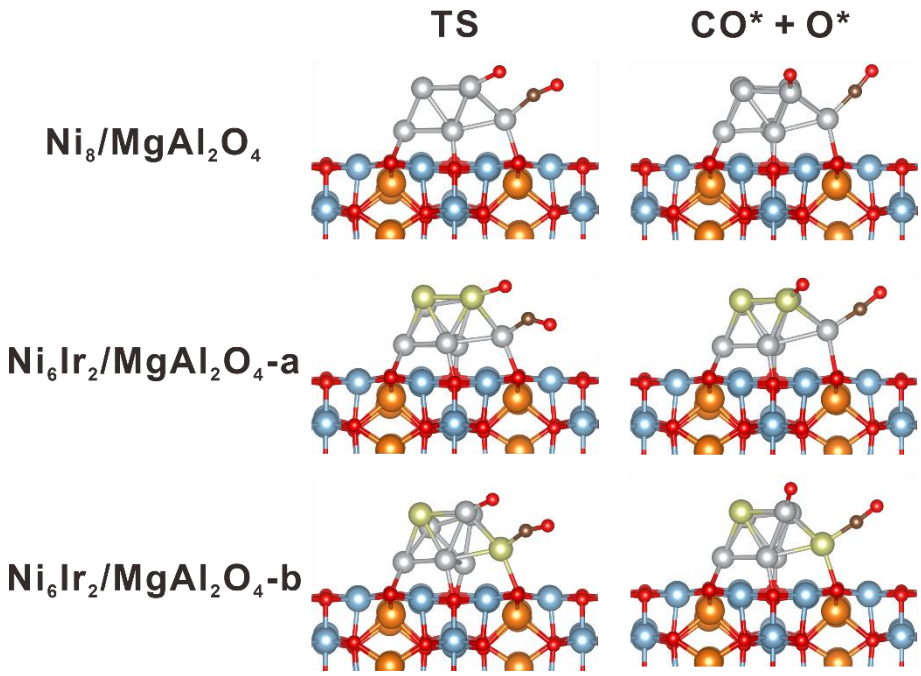

Fig. S17 DFT-optimized structures involved in CO_2 dissociation on $M_8/MgAl_2O_4$ catalysts.

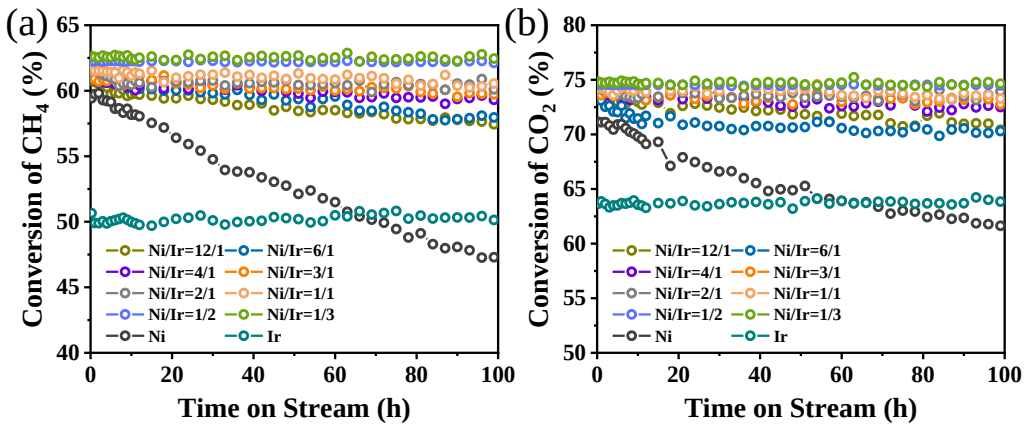

Fig. S18 Conversion of (a) CH_4 and (b) CO_2 over Ni-Ir/$MgAl_2O_4$ catalyst with different Ir contents for the 100-hour DRM test. Reaction conditions: 650 °C, CH_4/CO_2 = 1/1, GHSV = 40,000 mL·g^{-1}·h^{-1}, and 1 atm.

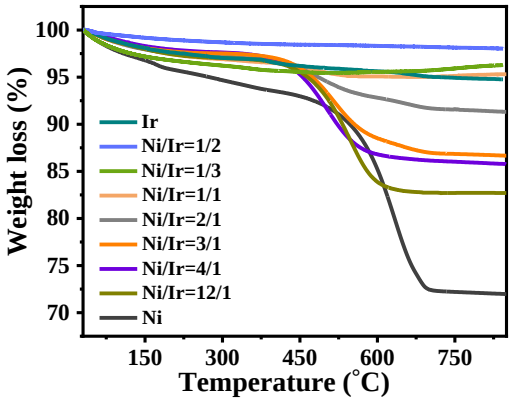

Fig. S19 TGA spectra of the spent Ni-Ir/$MgAl_2O_4$ catalysts with different Ir contents.

Tables

Table S1. XAFS data fitting for the $Ni_3Ir_1/MgAl_2O_4$ catalyst.

Edge	Shell	N	R/Å	$\Delta\sigma^2/Å^2$
Ni K-edge	Ni-Ni	3.6	2.46	0.00573
Ni K-edge	Ni-Ir	4.8	2.65	0.00573
Ir-K-edge	Ir-Ir	8.0	3.29	0.01291
Ir-K-edge	Ir-Ni	4.6	2.63	0.01291

238 Table S2. The comparison of the performance of dry reforming of methane with Ni-
239 based bimetallic catalysts.

Catalyst	Gas composition	GHSV $L \cdot g^{-1} \cdot h^{-1}$	Temp.	CH_4 Conv.	CO_2 Conv.	CH_4 Conv. rate $L \cdot g^{-1} \cdot h^{-1}$	CO_2 Conv. Rate $L \cdot g^{-1} \cdot h^{-1}$
$NiIr/MgAl_2O_4$ [this work]	CH_4/CO_2=1/1	40	650	62.5	74.6	12.5	14.9
$NiIr/MgAl_2O_4$ [this work]	CH_4/CO_2=1/1	40	700	77.4	88.6	15.5	17.7
$NiIr/MgAl_2O_4$ [this work]	CH_4/CO_2=1/1	40	750	84.7	93.9	16.9	18.8
$NiIr/MgAl_2O_4$ [this work]	CH_4/CO_2=1/1	40	800	90.4	97.0	18.1	19.4
$NiPd/SiO_2$-OA [12]	CH_4/CO_2=1/1	24	700	65	76	7.8	9.1
PdNi/MgO [13]	CH_4/CO_2/He=1/1/12	70	600	48	47	2.4	2.5
PdNi/MgO [13]	CH_4/CO_2/He=1/1/12	70	750	97	96	4.9	4.8
$PtNi/Al_2O_3$ [14]	CH_4/CO_2/He = 2/2/6	30	700	69	76	4.1	4.6
$PtNi/Al_2O_3$ [15]	CH_4/CO_2=1/1	7	750	79	95	2.77	3.3
RhNiCo/ ZrO_2/Al_2O_3 [16]	$CH_4/CO_2/N_2$=7/7/1	45	800	67.6	71.8	14.2	15.1
$CoNi/CeO_2$ [17]	$CH_4/CO_2/N_2$=3/3/4	12	650	50	59	1.8	2.1
$NiCo/Al_2O_3$ [18]	CH_4/CO_2=1/1	36	700	67	71	12.1	12.8
NiCu/Mg(Al)O [19]	$CH_4/CO_2/N_2$=1/1/2	60	600	52	63	7.8	9.5
$GdNi/Y_2O_3$ [20]	$CH_4/CO_2/N_2$=17/17/6	8	700	78	73	2.7	2.5

240

Supplementary References

1 Li W. *et al.* Stable platinum nanoparticles on specific $MgAl_2O_4$ spinel facets at high temperatures in oxidizing atmospheres. *Nat. Commun.* **4**, 2481, doi: 10.1038/ncomms3481 (2013).

2 Kresse, G. & Furthmüller, J. Efficiency of ab-initio total energy calculations for metals and semiconductors using a plane-wave basis set. *Comput. Mater. Sci.* **6**, 15-50, doi:10.1016/0927-0256(96)00008-0 (1996).

3 Kresse, G. & Furthmüller, J. Efficient iterative schemes for ab initio total-energy calculations using a plane-wave basis set. *Phys. Rev. B* **54**, 11169-11186, doi:10.1103/PhysRevB.54.11169 (1996).

4 Kresse, G. & Hafner, J. Ab initio molecular dynamics for open-shell transition metals. *Phys Rev B* **48,** 13115-13118, doi:10.1103/PhysRevB.48.13115 (1993).

5 Kresse, G. & Hafner, J. Ab initio molecular-dynamics simulation of the liquid-metal-amorphous-semiconductor transition in germanium. *Phys. Rev. B* **49**, 14251-14269, doi:10.1103/PhysRevB.49.14251 (1994).

6 Perdew, J. P., Burke, K. & Ernzerhof, M. Generalized gradient approximation made simple. *Phys. Rev. Lett.* **77**, 3865-3868, doi:10.1103/PhysRevLett.77.3865 (1996).

7 Kresse, G. & Joubert, D. From ultrasoft pseudopotentials to the projector augmented-wave method. *Phys. Rev. B* **59**, 1758−1775, doi:10.1103/PhysRevB.59.1758 (1999).

8 Grimme, S., Ehrlich, S., & Goerigk, L. Effect of the damping function in dispersion corrected density functional theory. *J. Comput. Chem.* **32**, 1456−1465, doi:10.1002/jcc.21759 (2011).

9 Henkelman, G. & Jónsson, H. Improved tangent estimate in the nudged elastic band method for finding minimum energy paths and saddle points. *J. Chem. Phys.* **113**, 9978-9985, doi:10.1063/1.1323224 (2000).

10 Krukau, A. V. *et al.* Influence of the exchange screening parameter on the performance of screened hybrid functionals. *J. Chem. Phys.* **125**, 224106, doi:10.1063/1.2404663 (2006).

11 Henkelman, G. & Jónsson, H. A dimer method for finding saddle points on high dimensional potential surfaces using only first derivatives. *J. Chem. Phys.* **111**, 7010-7022, doi:10.1063/1.480097 (1999).

12 Pan, C., Guo, Z., Dai, H., Ren, R. & Chu, W. Anti-sintering mesoporous Ni–Pd bimetallic catalysts for hydrogen production via dry reforming of methane. *Int. J. Hydrog. Energy* **45**, 16133-16143, doi:10.1016/j.ijhydene.2020.04.066 (2020).

13 Singha, R. K., Shukla, A., Sandupatla, A., Deo, G. & Bal, R. Synthesis and catalytic activity of a Pd doped Ni–MgO catalyst for dry reforming of methane. *J. Mater. Chem. A* **5**, 15688-15699, doi:10.1039/c7ta04452f (2017).

14 García-Diéguez, M., Pieta, I. S., Herrera, M. C., Larrubia, M. A. & Alemany, L. J. Nanostructured Pt- and Ni-based catalysts for CO_2-reforming of methane. *J. Catal.* **270**, 136-145, doi:10.1016/j.jcat.2009.12.010 (2010).

15 de Miguel, S. R. *et al.* Influence of Pt addition to Ni catalysts on the catalytic performance for long term dry reforming of methane. *Appl. Catal. A-Gen.* **435-436**, 10-18, doi:10.1016/j.apcata.2012.05.030 (2012).

16 Al-Fatesh, A. *et al.* Rh promoted and ZrO_2/Al_2O_3 supported Ni/Co based catalysts: High activity

for CO_2 reforming, steam–CO_2 reforming and oxy–CO_2 reforming of CH_4. *Int. J. Hydrog. Energy* **43**, 12069-12080, doi:10.1016/j.ijhydene.2018.04.152 (2018).

17 Turap, Y. *et al.* Co–Ni alloy supported on CeO_2 as a bimetallic catalyst for dry reforming of methane. *Int. J. Hydrog. Energy* **45**, 6538-6548, doi:10.1016/j.ijhydene.2019.12.223 (2020).

18 Siang, T. J. *et al.* Hydrogen production from CH_4 dry reforming over bimetallic Ni–Co/Al_2O_3 catalyst. *J. Energy Inst.* **91**, 683-694, doi:10.1016/j.joei.2017.06.001 (2018).

19 Song, K. *et al.* Effect of alloy composition on catalytic performance and coke-resistance property of Ni-Cu/Mg(Al)O catalysts for dry reforming of methane. *Appl. Catal. B-Environ.* **239**, 324-333, doi:10.1016/j.apcatb.2018.08.023 (2018).

20 Al-Fatesh, A. S. Promotional effect of Gd over Ni/Y_2O_3 catalyst used in dry reforming of CH_4 for H_2 production. *Int. J. Hydrog. Energy* **42**, 18805-18816, doi:10.1016/j.ijhydene.2017.06.165 (2017).